JPhys Photonics

PURPOSE-LED PUBLISHING™

PAPER • OPEN ACCESS

Near-field nano holographic tomography with chemical contrast exploiting low-dimensionality constraints

To cite this article: Johannes Gruen *et al* 2026 *J. Phys. Photonics* **8** 025043

Journal of Physics: Photonics

OPEN ACCESS

RECEIVED
7 April 2026

REVISED
13 May 2026

ACCEPTED FOR PUBLICATION
27 May 2026

PUBLISHED
22 June 2026

PAPER

Near-field nano holographic tomography with chemical contrast exploiting low-dimensionality constraints

Johannes Gruen[1,*], Johannes Dora[1], Thea Engler[1], Martin Seyrich[1], Andreas Schropp[1], Jakob Soltau[3], Markus Osterhoff[3], Thomas L Sheppard[4,5], Tim Salditt[3], Christian G Schroer[1,2,6] and Johannes Hagemann[1]

[1] Center for X-ray and Nano Science CXNS, Deutsches Elektronen Synchrotron DESY, Hamburg, Germany
[2] Center for Hybrid Nanostructures, Institute for Nanostructure and Solid-State Physics, University of Hamburg, Hamburg, Germany
[3] Institute for X-ray Physics, University of Göttingen, Göttingen, Germany
[4] Institute of Chemical Technologies and Analytics, TU Wien, Wien, Austria
[5] Institute for Chemical Technology and Polymer Chemistry, Karlsruhe Institute of Technology, Karlsruhe, Germany
[6] Helmholtz Imaging, Deutsches Elektronen-Synchrotron DESY, Hamburg, Germany
[*] Author to whom any correspondence should be addressed.

E-mail: johannes.gruen@desy.de

Keywords: 3D XANES, X-ray inline holography, spectro nano tomography

Abstract

X-ray absorption near-edge structure (XANES) spectroscopy is key to understanding functional materials. We present, to our knowledge, the first use of hard x-ray near-field holography (NFH) for three-dimensional (3D), spatially resolved XANES. While NFH provides lensless imaging with an adjustable field of view, it entails complex reconstruction. Our method jointly reconstructs NFH data acquired at multiple energies and enforces a low-dimensional spectral model based on the physically motivated assumption that each voxel spectrum is a linear combination of a small number of constituents. We demonstrate the approach on a mixed metal oxide catalyst particle, achieving accurate spectral reconstruction and revealing 3D chemical heterogeneity. XANES in NFH mode has the potential to enable nano-scale *in-operando* XANES microscopy with a large field of view.

1. Introduction

Three-dimensional (3D) x-ray absorption near-edge structure (XANES) microscopy has emerged as a powerful tool for probing the distribution of chemical states at the micro- and nanoscale [1–4]. XANES provides access to the oxidation state and local projected density of free states of a given element, enabling detailed chemical mapping within complex heterogeneous systems. Understanding these nanoscale chemical variations is critical for optimizing the performance of functional materials such as catalysts, batteries, and semiconductors [5–7].

Several synchrotron-based methods have been developed to combine XANES with spatially resolved imaging [8, 9]. Each method offers specific advantages and limitations in terms of spatial resolution, acquisition speed, and contrast mechanisms. Full-field TXM-based XANES tomography enables chemical-state mapping in 3D by collecting tomographic projections across an absorption edge, producing a XANES spectrum per voxel [10, 11]. It provides direct absorption contrast acquisition over the full field of view. However, spatial resolution is limited by the quality of the objective optics and flux is reduced by the TXM setup leading to longer measurement times. Moreover, this approach typically provides a smaller field of view than other magnifying full-field techniques due to the experimental geometry. Scanning-based methods such as spectro-ptychographic imaging [12, 13] and tomography have advanced XANES imaging by combining the high spatial resolution of ptychographic tomography with spectral information from multiple energies [14, 15]. These methods offer sub-30 nm resolution, ideal for identifying chemical domains in nanostructured materials. As these methods are scanning-based, they are slower than full-field methods but lead to higher resolution. Gao *et al* overcame this limitation by

measuring a fraction of the required angles according to Crowther criterion at each energy and using an assumption about the low-dimensionality of the signal to fill the remaining angles using a combination of principle component analysis (PCA) and simultaneous algebraic reconstruction technique (SART) [16, 17].

Ptychographic and holographic tomography typically recover the phase shift, because at nanoscale resolution it yields a stronger signal than absorption contrast. Phase shift and absorption are related by Kramers–Kronig relation, hence reconstructing phase shift or absorption spectra is equivalent for subsequent analysis [18, 19]. Consequently, reconstruction of the phase shift provides access to oxidation states and the local projected density of free states that is similar to that obtained from absorption-based measurements. But alas, phase measurements require an additional reconstruction step because the phase information is lost during measurement and only intensities are recorded. This increases pipeline complexity, as phase retrieval is an ill-posed, nonlinear problem and can, in some cases, produce lower-quality reconstructions than absorption-based measurements. In particular, recovering low spatial frequencies is non-trivial as they are partly encoded by the forward model, which can introduce fluctuations across energies that make subsequent XANES analysis impossible unless additional constraints are imposed on the reconstruction algorithm.

In this work, we demonstrate that near-field holotomography [20–22] across energies fulfills the requirements of XANES tomography. Namely, it enables fast measurements, which might be suitable for capturing reaction dynamics in future experiments, provides high resolution, and offers a scalable field of view, allowing the study of samples more representative of real industrial materials. For data processing we develop a novel reconstruction algorithm, which reconstructs the complex refractive index jointly across energies and allows to enforce a low-dimensional representation of the spectra. Incorporating a low-dimensionality constraint stabilizes the reconstructed spectra by enforcing consistency across energies. This specifically removes the low-frequency fluctuations, enabling subsequent XANES analysis. The low-dimensional constraint relies on the prior knowledge that the sample can be described by a linear combination of a few reference spectra, which are not necessarily determined. Since a typical XANES measurement is conducted across an absorption edge of a given element of interest, it is a linear combination of a small set of specific spectra corresponding to chemical states present in the sample. While a common approach would be to take the reference spectra and simply fit linear coefficients, we instead project the retrieved phases at each step into a low-dimensional space and back, ensuring spatial consistency across energies. This has the advantage of avoiding biases towards certain spectra. Experiments were conducted at the GINIX endstation at the beamline P10 (PETRA III, DESY, Hamburg, Germany) [23]. As a sample, Bi–Mo–Fe–Co, a complex mixed-metal oxide (MMO), is used due to its relevance in many industrial chemical synthesis processes and presence of various crystalline and amorphous phases with different oxidation states even among the same elements, providing an appropriate test sample [24]. Measurements were conducted at the cobalt K-edge, from 7706.5 eV to 7746.5 eV. Each tomogram includes 1500 projections equally distributed over 180 degrees, with fine energy sampling near the Co K-edge.

2. Data and methods

2.1. Sample

The sample is a 4-component MMO catalyst of Bi–Mo–Co–Fe-oxides with the elemental composition 4.2/50.0/33.3/12.5 wt.% respectively. The synthesis and pre-treatment procedure is detailed in previous work (HS-U catalyst composition) [25]. The catalyst particle studied here was synthesized and then calcined in static air for 5 h at 320 °C. Detailed characterization of the catalyst system including elemental analysis, Raman spectroscopy, synchrotron powder XRD and XAS can be found in previous work [25]. The catalyst particle was selected and placed on a tomography pin using a dual beam FIB-SEM instrument via micromanipulation by the DESY NanoLab. An electron microscopy image is shown in figure 2(a) and a flat-field corrected holographic measurement in figure 2(b). The sample has a diameter of around 34 μm and it is assumed that Co is present in four different chemical states within the sample.

2.2. Data acquisition

The measurements were conducted at beamline P10 of PETRA III (DESY, Hamburg) using the GINIX x-ray waveguide setup [23, 26, 27]. The beamline is equipped with a KB mirror, a waveguide, an Andor Zyla sCMOS detector with 2160 × 2560 pixels of size Δ_x 6.5 μm, and a 15 μm Gadox scintillator. The photon energy was selected by a Si(111)-monochromator, which was calibrated using a cobalt foil. The

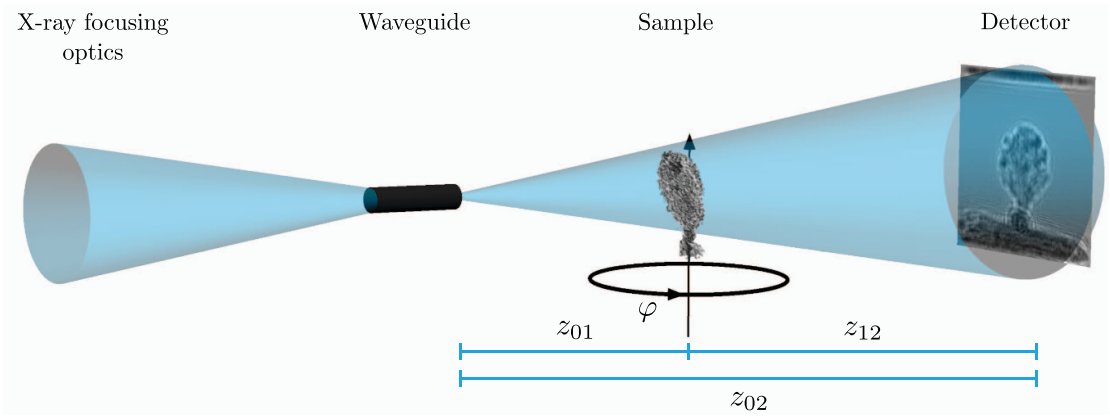

Figure 1. Schematic representation of the measurement setup. The incoming x-ray beam is focused by a Kirkpatrick–Baez (KB) mirror system onto a waveguide, which spatially filters the beam and generates a coherent wavefront. The sample is placed in the resulting cone beam at a distance z_{01} from the waveguide. After interaction with the sample, the x rays propagate to the detector, which is positioned at a distance z_{12} downstream of the sample. By acquiring projections at multiple rotation angles φ, a holotomographic dataset is obtained.

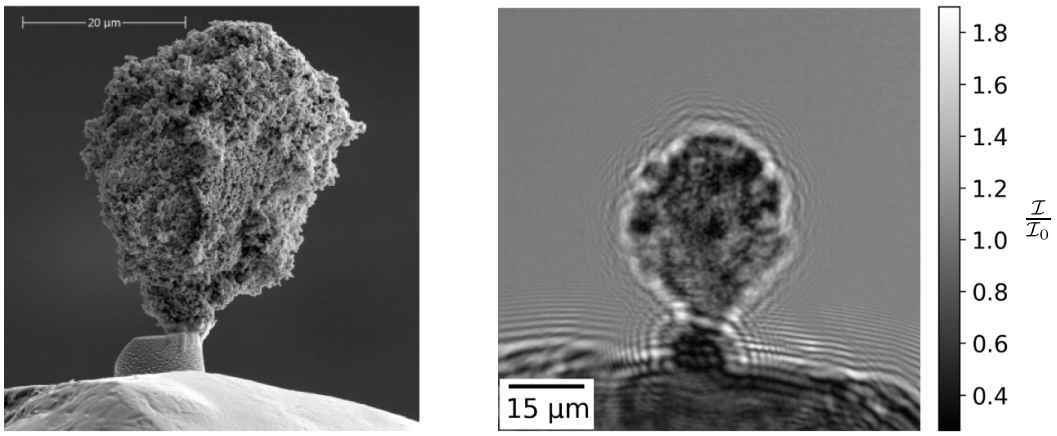

(a) Mounted catalyst with a diameter of 34 µm measured with an electron microscope. Image was taken by the NanoLab.

(b) Flat-field corrected hologram of catalyst.

Figure 2. Images of the sample using different modalities.

waveguide with a channel width of 100 nm, functioning as a non-dispersive x-ray optics, ensures that the effective source position remains fixed while varying the x-ray photon energy. The waveguide channels of 100 nm width and depth (nominal values) were fabricated by e-beam lithography (Eulitha, Switzerland) in Si(100) wafers, capped by wafer bonding at IRP, and diced to a channel length of 1.75 mm optical thickness, as described in [28]. The exit intensity was around 2.5×10^9 ph·s^{-1}, with exact values depending on the alignment state.

The fixed source position leads to a constant geometry, i.e. the magnification M is constant, which is advantageous for subsequent joint phase retrieval, as the Fresnel number is only depending on the photon energy in this case. The sample is placed $z_{01} = 62.2$ mm behind the exit of the waveguide and propagated for $z_{12} = 5.048$ m, as subsequent analysis shows. This leads to an overall magnification $M = z_{02}/z_{01} \approx 82$.

A total of 32 tomograms were acquired across a photon energy range from 7706.5 eV to 7746.5 eV. The effective Fresnel number is defined as

$$\mathrm{Fr}_{\mathrm{eff}} := \frac{\Delta_x^2}{M\lambda z_{12}}, \tag{1}$$

where Δ_x denotes the pixel size of the detector, λ the wavelength, and z_{12} the distance from sample to detector, as depicted in figure 1. Hence, it is directly related to the photon energy, leading to an effective Fresnel number range of 6.33×10^{-4} to 6.363×10^{-4}.

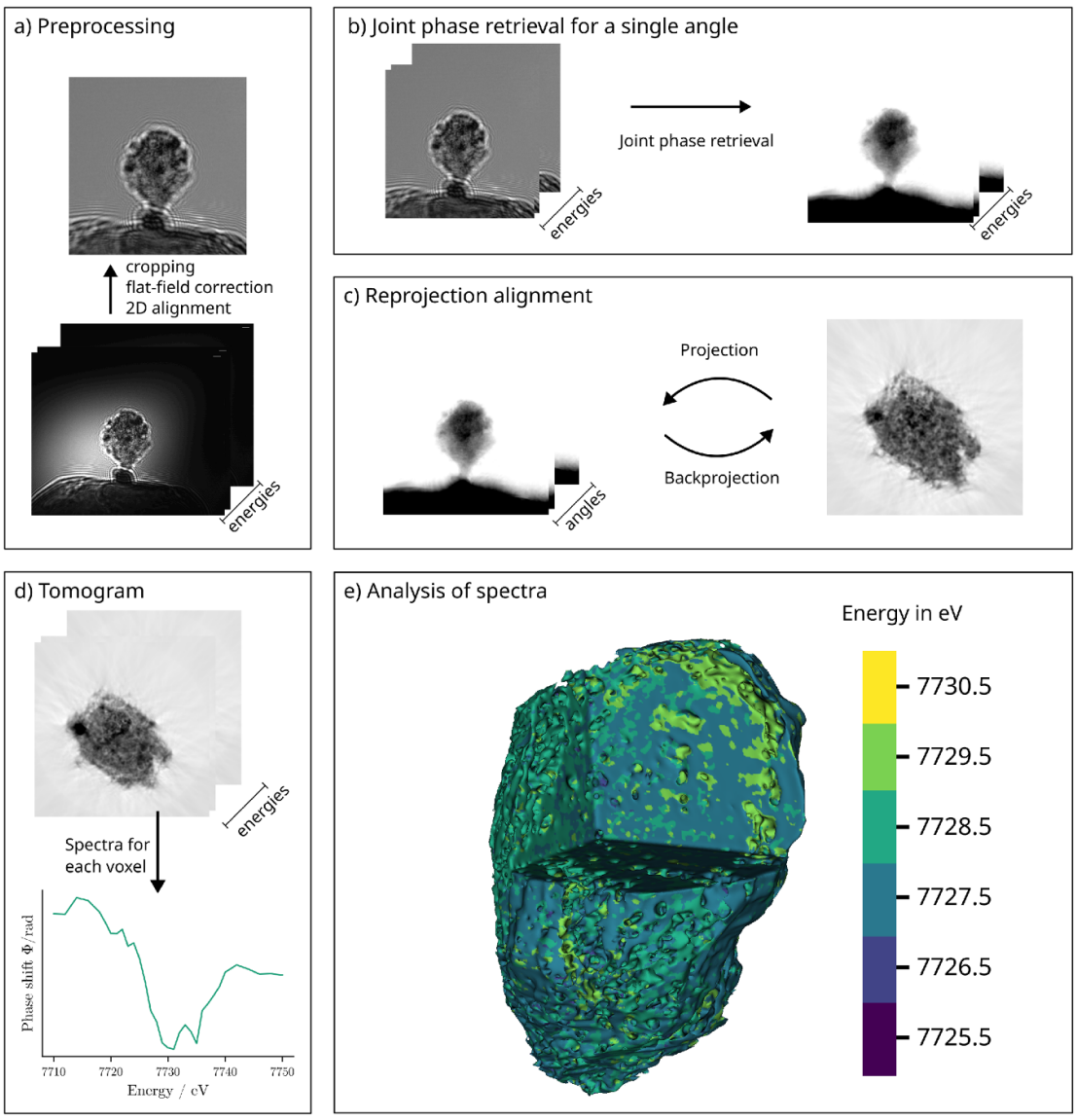

Figure 3. Overview of the processing pipeline. The pipeline consists of five main steps: (a) 2D alignment for each angle over all energies. (b) Joint phase retrieval for each angle over all energies. (c) Reprojection alignment is performed for all energies. (d) Tomograms are generated for all energies, leading to a spectra per voxel. (e) Analysis of the computed spectra. In this case the minimal phase shift is computed for each voxel. Most minima are clustered around 7726.5 eV.

Between each tomogram, the waveguide alignment was verified. Closer to the expected absorption edge at 7724.5 eV, measurements were conducted in 1 eV steps, while at energies approximately 10 eV away from the absorption edge (7706.5 eV to 7713.5 eV and 7736.5 eV to 7746.5 eV) the spectrum was sampled in 2 eV steps. Each tomogram comprises 1500 projections, equally distributed over a half-circle angular range. To enable flat-field correction, 50 flat-field images were recorded both before and after each tomogram.

The measurement time for a single tomogram is approximately 32 min. This results in a net measurement time of 17 h:36 min. Due to the need to reacquire measurements and realign the waveguide, the total scan time including this overhead was approximately 34 h. The measurement time can be significantly reduced by collecting sparse measurements in the energy domain and adopting a strategy similar to that proposed by Gao *et al* [15].

2.3. Data analysis

The data processing pipeline is depicted in figure 3. It consists of five steps, which are preprocessing, joint phase retrieval, reprojection alignment, tomogram generation, and finally analysis of the reconstructed spectra. All the steps are explained within the following.

2.3.1. Preprocessing

As a first step the holograms $\{\mathcal{I}_{\varphi,E} \mid E \in \mathcal{E}\}$ for a single angle φ across all energies $\mathcal{E}$ are registered to the lowest energy projection using rigid body registration [29]. Non illuminated regions on the detector were cropped, resulting in a image size of 1024 $\times$ 1024. PCA based flat-field correction is then applied to the cropped images, under the assumption that the probe is compensated for by the correction [30, 31]. This is followed by estimation of the normalization constant A_0, which normalizes the background to 1 [32]. For this purpose, Segment Anything 2 is used to segment the foreground from the background [33].

To estimate the scanning geometry we perform autofocusing, i.e. estimate the distance from the waveguide to the object for the first hologram at each energy [34]. The estimated distances is 62.2 ± 0.2 mm for all energies. As the distance is assumed to be energy-independent, we use the mean value for all reconstructions.

2.3.2. Joint phase retrieval

The interaction of x-rays with matter results in a phaseshift and absorption, characterized by the complex refractive index, which is defined as

$$n(E,x,y,z) = 1 - \delta(E,x,y,z) + \mathrm{i}\beta(E,x,y,z), \tag{2}$$

where (x,y,z) denotes the spatial position, E the photon energy in eV, $\delta \in \mathbb{R}_{\leqslant 0}$ the phase shift, and $\beta \in \mathbb{R}_{\geqslant 0}$ the absorption. Propagation of the wave field through free space is described by the Fresnel approximation

$$\mathcal{D}_{\mathrm{Fr}_{\mathrm{eff}}} = \mathcal{F}^{-1}\left[\exp\left(\mathrm{i}\pi \frac{k_x^2 + k_y^2}{\mathrm{Fr}_{\mathrm{eff}}}\right) \cdot \mathcal{F}(\Psi)\right], \tag{3}$$

where $\mathcal{F}$ and $\mathcal{F}^{-1}$ denote the Fourier transform and its inverse, $\mathrm{Fr}_{\mathrm{eff}}$ the effective Fresnel number and Ψ is the wave field behind the object in thin object approximation [35]. The algorithm by Dora *et al* comprises several stages designed to mitigate the common limitations encountered in phase retrieval. First, compliance with the Fourier-transform-sampling requirements is ensured through the application of mirroring, padding, and fading. Second, high-frequency components are attenuated via Gaussian smoothing, reflecting the fact that the forward operator $\mathcal{D}_{\mathrm{Fr}_{\mathrm{eff}}}$ is sensitive to the second spatial derivative: high-frequency features are reconstructed reliably, whereas low-frequency components are comparatively difficult to recover. Third, Nesterov acceleration is incorporated to enhance the reconstruction of low-frequency information. To prevent overshooting the imaginary part $\Im$ is regularized and high-frequency components of the Nesterov momentum are attenuated by Gaussian smoothing. Finally, a projection onto the respective constraint sets is performed to enforce physical validity. To further improve speed and convergence, the optimization is first performed on a multi-scale grid, i.e. first 16 times downsampled, then 4,2,1 times downsampled.

We adapt the algorithm of Dora *et al* [32] by performing phase retrieval over all energies and by introducing a projection of the object O into a lower-dimensional space at each iteration step, which leads to a joint reconstruction across energies. By incorporating the prior knowledge that the spectra can be represented in a low-dimensional subspace, we effectively reduce the degrees of freedom and thereby stabilize the reconstruction. The pseudocode of the proposed procedure is provided in Algorithm 1, and the corresponding hyperparameters are listed in table 1. For further explanations we refer to Dora *et al* [32].

As before, the predicted object $\tilde{O}_{k,E}$, where k is the iteration index and E the energy, is mirrored, padded, faded, and Gaussian-smoothed. A Nesterov-accelerated gradient step is then performed. Since the phase is negative while the absorption is positive in the hard x-ray regime, a projection operator $\mathcal{P}_{\Omega_p}$ projects onto the respective sets. This update step is performed for each energy.

To incorporate prior knowledge, i.e. that the absorption and phase spectra are low-dimensional, we apply singular value decomposition (SVD). Therefore, the foreground is estimated from the flat-field corrected holograms using Segment Anything 2, which is able to select the roundish particle and does not select the base. To include the whole foreground a dilation of 50 pixels is applied. The foreground of the updated object estimates $\Omega = \{\tilde{O}_{k,E} \mid E \in \mathcal{E}\}$ is then selected, and separate SVDs are calculated for the phase and absorption parts, treating energies as features and pixels as samples. The N SVD components with the highest absolute contribution are kept and the remaining are set to zero, i.e. $S = \mathrm{Diag}(\sigma_1, \ldots, \sigma_N, 0, \ldots, 0)$. Leading to a filtered estimation

$$\tilde{\Omega} = USV^{\top} \tag{4}$$

Algorithm 1. Joint phase retrieval with low-dimensionality prior.

Input: Preprocessed measurements $\{\mathcal{I}_E \mid E \in \mathcal{E}\}$, initial guess $\tilde{O}_{0,E}$, inital nesterov state $g_{0,E} = 0\, k = 0$

Hyperparameters: For each scaling stage $j \in \{0, \ldots, J\}$:

- Update rates η_j for gradient step
- Nesterov operator τ_j
- Nesterov momentum γ_j
- Gaussfilter coefficients σ_j
- L_2 regularization weight β_j

Output: Approximated solution $\tilde{O}^\star$

For $j \leftarrow 0$ **To** J **do**

  Repeat

    For each $E \in \mathcal{E}$ **do**

      $\tilde{O}'_{k,E} \leftarrow \text{gauss}_{\sigma_j}\Big(\text{fade}\big(\text{pad}\big(\text{mirr}(\tilde{O}_{k,E})\big)\big)\Big)$; // `preprocess`

      $y_{k+1,E} \leftarrow \tilde{O}'_{k,E} - \gamma_j \tau_j g_{k,E}$; // `Nesterov extrapolation`

      $g_{k+1,E} \leftarrow$

      $\gamma_j \tau_j g_{k,E} + \eta_j \nabla \left[\frac{1}{2} \left\| |\mathcal{D}_{\text{Fr}_\text{eff}}(y_{k+1,E})| - \sqrt{S^j_\downarrow \mathcal{I}_E} \right\|_2^2 + \frac{\beta_j}{\eta_j} \|\Im(y_{k+1,E})\|_2 \right]$;

      $n_{k+1,E} \leftarrow \mathcal{P}\left(\tilde{O}'_{k,E} - g_{k+1,E}\right)$; // `projection on constraints`

      $\tilde{O}_{k+1,E} \leftarrow \text{cutfov}(n_{k+1,E})$; // `crop back to FOV`

    Select foreground from $\{\tilde{O}_{k+1,E} \mid E \in \mathcal{E}\}$;

    For phase, absorption **do**

      Compute SVD (U, S, V) of foreground;

      Retain top N components of S by magnitude;

      forground $(\tilde{O}_{k+1}) \leftarrow USV^\top$; // `projection`

      background $(\tilde{O}_{k+1}) \leftarrow 0$;

    $k \leftarrow k + 1$;

  until stopping criterion reached;

  // `Change downsampling / update multi-scale level`

return $\tilde{O}_{k+1}$

Table 1. Hyperparameters for the joint phase-retrieval algorithm: η_j is the update strength, γ_j the momentum operator, σ_j and τ_j the smoothing operators given by the full width at half maximum separately for real and imaginary part, and β_j the regularization weight on the imaginary part of the refractive index. Regularization of the imaginary part is necessary, since an overestimation by the momentum operator, would lead to almost no propagated signal and therefore would destabilize the reconstruction. Both Gaussian smoothing operators are necessary to prevent unplausible high spatial frequency. Higher values would lead to smoothed reconstructions and vice versa.

j	Iter.	$S^{\{j\}}_\downarrow$	η_j	γ_j	β_j	σ_j	τ_j
0	1000	16×	1	1	1	0/1i	0/1i
1	100	4×	1	1	0.06	2/2i	2/2i
2	100	2×	1	0.8	0.06	4/4i	2/6i
3	100	1×	1	0.8	0	0/0i	0/0i

for phase and absorption, where $U \in \mathbb{R}^{m \times m}$ is a unitary matrix, $S \in \mathbb{R}^{m \times n}$ is a rectangular diagonal matrix, and $V \in \mathbb{R}^{n \times n}$ is a unitary matrix, where $n = \#(\text{pixels})$ and $m = \#(\text{energies})$. The filtered phase and absorption values are then used to initialize the next iteration $k+1$.

For the analysis we have measured $m = 32$ energies and have chosen $N = 6$ to be able to represent 4 oxidation states and some unknown effects. This procedure reduces the degrees of freedom without introducing unwanted biases into the reconstruction, i.e. unlike dictionary-based approaches that use reference spectra and estimate only the coefficients [36].

Additionally, a support constraint is applied using the foreground and selecting the base manually, i.e. all values which are not within the constrained mask are projected to zero, as no object should be within this region.

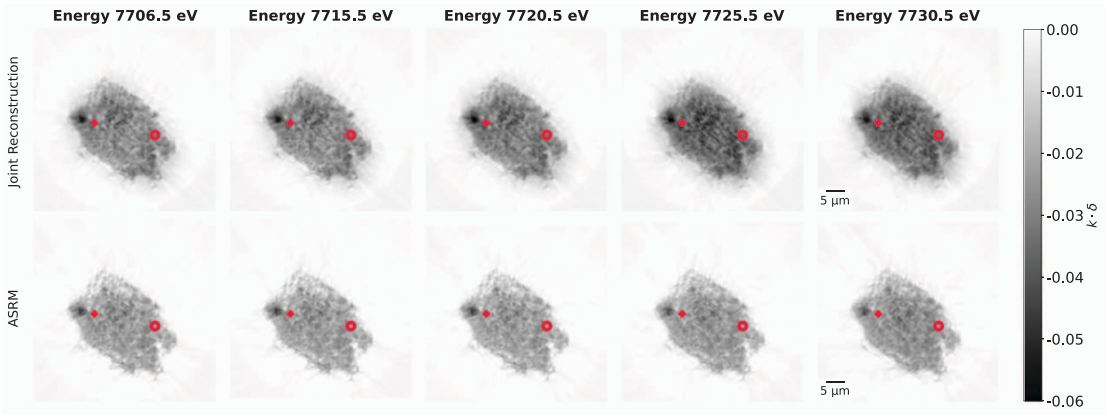

(a) A single tomographic slice at various energies for the proposed joint reconstruction (top) and the state of the art ASRM method (bottom). The joint reconstruction shows slightly higher phase shift values and greater contrast between energies. The circle and cross indicate two voxels whose respective spectra (also marked by ticks using circles and crosses) are shown below.

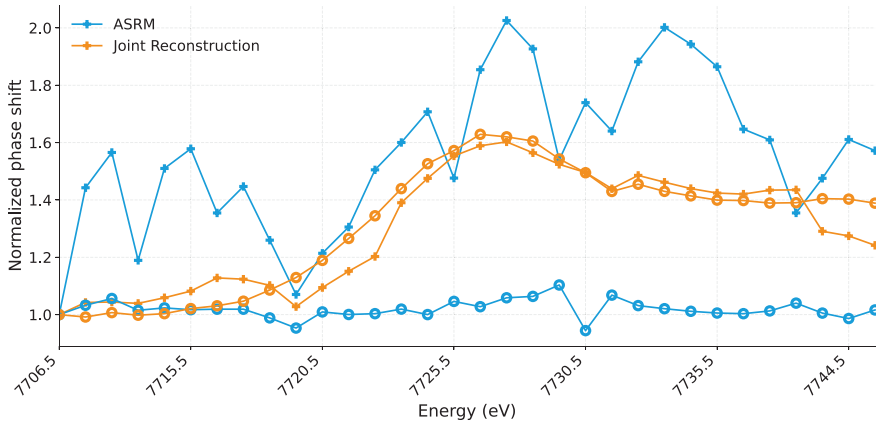

(b) Normalized phase shift spectra of the two labeled voxels from (a). Orange lines represent the joint reconstruction, while blue lines represent ASRM based independent reconstructions. Spectra are normalized by their respective maximum phase shift values for comparability. Independent reconstructions yield noisy spectra with no clear trend, whereas coupled reconstructions produce smoother, more coherent results.

Figure 4. Tomographic slice of phase shifts and corresponding voxel spectra.

2.3.3. Alignment for tomography projections

To reconstruct the tomograms, we perform reprojection alignment [37] for all energies. Since the projections are pre-registered across energies, it should be sufficient to perform reprojection alignment on a single energy and apply the calculated transformation to all other tomograms. Afterwards we analyzed the variance of the dx, dy shifts for each angle across the tomograms as a sanity check. As the standard deviation is constantly small (below 0.25 pixels), we take the mean value of predicted shifts and apply this to all projections. The reprojection alignment is shown in figure 3(c).

For reprojection alignment, we use a custom `Python` implementation. The method iteratively performs filtered backprojection and reprojection, aligning the phase images to the reprojected images using translation-based registration [37]. We use `ANTs` for image registration [29] and `Tomosipo` [38] based on `ASTRA` [39] for filtered backprojection. To improve convergence speed, a multiresolution scheme is applied: the input images are downsampled at three levels $(4, 2, 1)$ to first align coarser features before refining to finer details.

3. Results

Figure 4(a) presents a single tomographic slice reconstructed at different x-ray energies using the proposed method and, for comparison, the state-of-the-art ASRM method which is extended in this work.

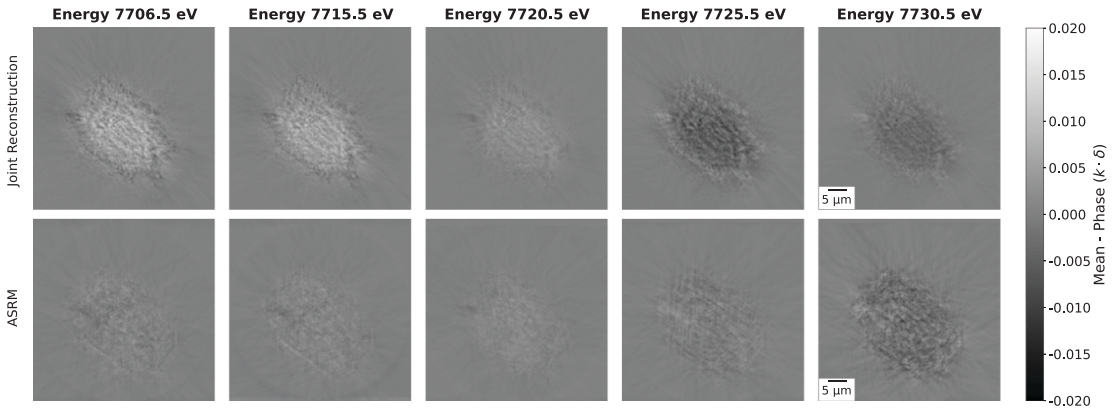

Figure 5. Differences between mean phase shift and respective energy phase shift. The independent reconstruction shows no clear pattern, whereas the joint reconstruction reveals distinct structures, indicating the presence of spatially correlated features.

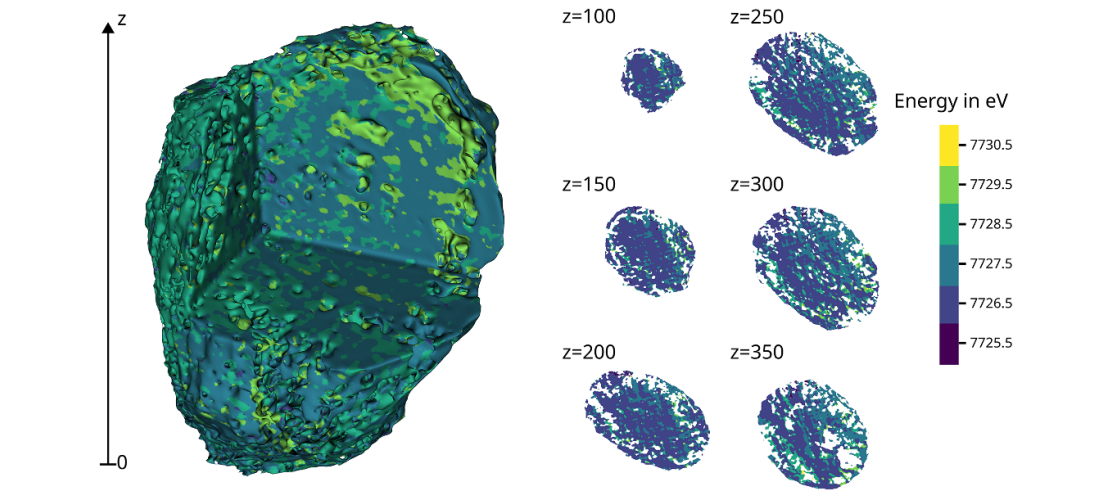

Figure 6. Left 3D rendering with cutting plane. Right: Several slices. The colorcoding denotes the energy with the minimal phase shift.

The stability of most structural features across the energy range indicates that the phase retrieval, reprojection alignment, and tomographic reconstruction have been successful. Although independently reconstructed images appear to exhibit higher contrast than those obtained with the joint approach, Fourier ring correlation analysis shows that both reconstruction methods achieve a spatial resolution of 79 nm according to the half-bit criterion [40]. Additionally, the overall structural consistency across energies is improved, as shown in the difference maps between the respective energy and the mean phase shift over all energies in figure 5. The difference maps of the joint reconstruction appear highly structured relative to those of the independent reconstructions, indicating suppressed low-frequency fluctuations and hence increased reconstruction stability. Moreover, the differences between the mean and the respective energy are larger for the joint reconstruction than for the independent reconstructions. We attribute this to reduced low-frequency errors, which lead to more consistent reconstructed phase-shift projections across angles.

When comparing the spectra of the two marked voxels, we observe that this results in more consistent and physically plausible spectral behavior, whereas the independently reconstructed spectra appear noisy and lack clear trends, as depicted in figure 4(b).

Additionally, we evaluated the minima of the phase-shift spectra as an indicator of the oxidation state, as shown in figure 6. Note that the analysis is based on phase-shift spectra and hence minima are of interest. Further, the minimum is correlated to the oxidation state, but is not an unique identifier. In approximately 80% of all voxels with a phase shift of at least -0.01 per energy, the minima lie within the range of 7725.5 eV to 7729.5 eV. In comparison, only a small fraction of voxels in the independently reconstructed tomograms exhibit minima within this expected range.

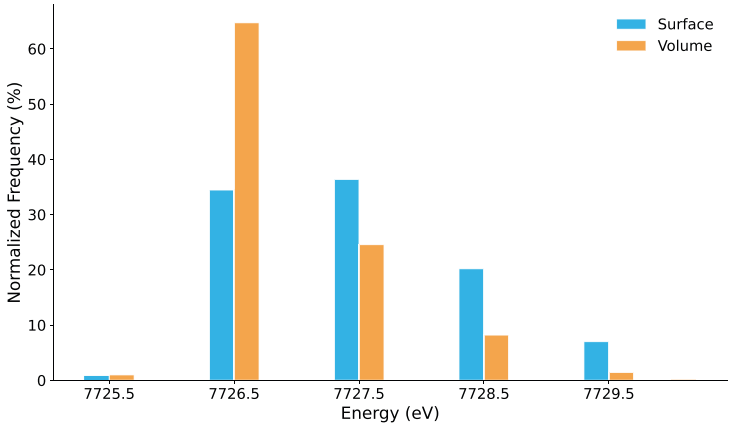

Figure 7. Distribution of minima of the phase shift on the surface in comparison to the overall distribution. Both distributions are normalized to 1. It becomes evident that the distribution shifts towards higher energies compared to the overall volume, which is physically plausible as the oxidation state increases at the surface.

To further validate the reconstructed spectra, we analyzed the minima on the particle surface and compared them with the overall distribution within the particle (figure 7). The surface was extracted using the marching cubes algorithm, retaining only the largest connected component to remove noisy artifacts. The histograms in figure 7 clearly indicate a shift towards higher oxidation states on the surface compared to the interior of the catalyst. As reactions are taking place on the surface this leads to higher oxidation states on the surface and hence, reduced catalyst performance.

4. Conclusion and outlook

In this work, we successfully reconstructed 3D-resolved spectral phase shift from near-field holography measurements. Using a new algorithm that enforces a low-dimensionality constraint on the retrieved spectra, we extracted spectral information without relying on any measured reference spectra. This enabled us to locate the position of the absorption edge and thus the oxidation state of Co in each voxel. The validity of this approach was demonstrated by observing an increased oxidation state at the surface of the material, which is a strong indicator for aging [11].

We note that the proposed method could also be applied to holographic measurements when no absorption edge is present. This offers an alternative to the commonly used multi-distance measurement technique for increasing signal diversity. Acquiring data at a single propagation distance over multiple energies would increase signal diversity while reducing alignment artifacts.

To further improve this method, both algorithmic and experimental developments are required. First, we will investigate extensions of the proposed algorithm, including the incorporation of prior knowledge in the form of measured reference spectra. Rather than enforcing a low-dimensional representation explicitly, such information could be included as an additional regularization term within a gradient-based optimization framework. Within the current work, we declined to use reference spectra, as this might bias the reconstructions towards the references, which might be flawed due to measurement errors. The proposed algorithm is fully data-driven omitting these caveats.

Second, we will explore sparse angular and energy sampling [1], which has the potential to significantly reduce acquisition time and thereby enable *in-operando* measurements.

Third, we will further validate the method on reference systems and assess its limitations, such as detection limits and the quantitative accuracy of phase-shift reconstructions. The current experiment does not allow such an analysis, since no well-characterized reference sample was measured. Therefore, we used the distribution of oxidation states as a surrogate measure for validity.

Combining the advantages of near-field holotomography, i.e. an adaptable FOV, phase sensitivity and single exposures, with the envisioned improvements above in a dedicated experiment would provide spectroscopists with a unique tool at 4th generation synchrotron radiation sources such as PETRA IV [41]. For PETRA IV, current estimates suggest that the measurement time will be reduced by a factor of 100. This would lead to a reduction in measurement time to around 10 minutes if all projections across all energies are taken, and to below 3 minutes if a sparse sampling strategy is used.

Additionally, the scanned sample volumes could be drastically increased which would yield better understanding of bulk material for relevant chemical processes.

Acknowledgments

We acknowledge DESY (Hamburg, Germany), a member of the Helmholtz Association HGF, for the provision of experimental facilities, and DASHH, Data Science in Hamburg—Helmholtz Graduate School for the Structure of Matter, for financial support. Parts of this research were carried out at PETRA III and DESY NanoLab. We would like to thank Satishkumar Kulkarni from NanoLab for FIB sample preparation. Data were collected at the GINIX setup located at beamline P10. We would like to thank Fabian Westermeier and Michael Sprung for assistance in using the experimental facilities at P10. Beamtime was allocated for proposal(s) I-20211269. This research was supported in part through the Maxwell computational resources operated at DESY and the innovation platform Hi-Acts under the grant of the HGF.

Data availability statement

The data that support the findings of this study are openly available at the following URL/DOI: https://zenodo.org/records/20552992 [42].

Funding

Helmholtz Association (ZT-I-PF-4-027 (SmartPhase)); Deutsche Forschungsgemeinschaft (DFG) - SFB 1441 - Project-ID 42 688 8090.

Author contributions

Johannes Gruen 0000-0002-9154-3929
Formal analysis (lead), Investigation (lead), Methodology (equal), Software (lead), Visualization (lead), Writing – original draft (lead), Writing – review & editing (lead)

Johannes Dora 0009-0001-4283-8499
Data curation (equal), Investigation (equal), Methodology (equal), Writing – review & editing (equal)

Thea Engler 0009-0006-8183-3603
Data curation (equal), Investigation (equal), Methodology (equal), Writing – review & editing (equal)

Martin Seyrich 0000-0002-4280-7924
Data curation (equal), Investigation (equal), Methodology (equal), Writing – review & editing (equal)

Andreas Schropp 0000-0002-8846-8585
Data curation (equal), Investigation (equal), Methodology (equal), Writing – review & editing (equal)

Jakob Soltau 0000-0003-1576-695X
Data curation (equal), Investigation (equal), Methodology (equal), Writing – review & editing (equal)

Markus Osterhoff 0000-0002-7865-515X
Data curation (equal), Investigation (equal), Methodology (equal), Writing – review & editing (equal)

Thomas L Sheppard 0000-0002-8891-985X
Conceptualization (equal), Data curation (equal), Investigation (equal), Methodology (equal), Project administration (equal), Resources (equal), Supervision (equal), Writing – review & editing (equal)

Tim Salditt 0000-0003-4636-0813
Project administration (equal), Resources (equal), Supervision (equal), Writing – review & editing (equal)

Christian G Schroer 0000-0002-9759-1200
Funding acquisition (equal), Investigation (equal), Methodology (equal), Project administration (equal), Resources (equal), Supervision (equal), Writing – review & editing (equal)

Johannes Hagemann 0000-0003-2768-9496
Conceptualization (equal), Funding acquisition (equal), Investigation (equal), Methodology (equal), Project administration (equal), Resources (equal), Supervision (equal), Writing – original draft (equal), Writing – review & editing (equal)

References

[1] Gao R, Zhang L, Tao F, Wang J, Du G, Xiao T and Deng B 2024 Transmission x-ray microscopy-based three-dimensional XANES imaging *Analyst* **149** 4506–13
[2] Becher J, Sanchez D F, Doronkin D E, Zengel D, Meira D M, Pascarelli S, Grunwaldt J-D and Sheppard T L 2021 Chemical gradients in automotive Cu-SSZ-13 catalysts for NOx removal revealed by operando x-ray spectrotomography *Nat. Catal.* **4** 46–53
[3] Price S W T, Ignatyev K, Geraki K, Basham M, Filik J, Vo N T, Witte P T, Beale A M and Mosselmans J F W 2014 Chemical imaging of single catalyst particles with scanning μ-XANES-CT and μ-XRF-CT *Phys. Chem. Chem. Phys.* **17** 521–9
[4] Alizadehfanaloo S 2024 High-resolution x-ray imaging of catalytic reactions by using x-ray absorption spectroscopy *PhD Dissertation* University of Hamburg
[5] Wang J *et al* 2025 Atomic to nanoscale chemical fluctuations: the catalyst for enhanced thermoelectric performance in high-entropy materials *Sci. Adv.* **11** eadt6298
[6] Naraprawatphong R, Chokradjaroen C, Thiangtham S, Yang L and Saito N 2022 Nanoscale advanced carbons as an anode for lithium-ion battery *Mater. Today Adv.* **16** 100290
[7] Nishida J, Chang P T S, Ye J Y, Sharma P, Wharton D M, Johnson S C, Shaheen S E and Raschke M B 2022 Nanoscale heterogeneity of ultrafast many-body carrier dynamics in triple cation perovskites *Nat. Commun.* **13** 6582
[8] Schroer C G *et al* 2003 Mapping the chemical states of an element inside a sample using tomographic x-ray absorption spectroscopy *Appl. Phys. Lett.* **82** 3360–2
[9] Hannemann S, Grunwaldt J-D, van Vegten N, Baiker A, Boye P and Schroer C G 2007 Distinct spatial changes of the catalyst structure inside a fixed-bed microreactor during the partial oxidation of methane over Rh/Al2O3 *Catal. Today* **126** 54–63
[10] Meirer F, Cabana J, Liu Y, Mehta A, Andrews J C and Pianetta P 2011 Three-dimensional imaging of chemical phase transformations at the nanoscale with full-field transmission x-ray microscopy *J. Synchrotron Radiat.* **18** 773–81
[11] Meirer F, Kalirai S, Morris D, Soparawalla S, Liu Y, Mesu G, Andrews J C and Weckhuysen B M 2015 Life and death of a single catalytic cracking particle *Sci. Adv.* **1** e1400199
[12] Beckers M, Senkbeil T, Gorniak T, Reese M, Giewekemeyer K, Gleber S-C, Salditt T and Rosenhahn A 2011 Chemical Contrast in Soft x-ray Ptychography *Phys. Rev. Lett.* **107** 208101
[13] Hoppe R, Reinhardt J, Hofmann G, Patommel J, Grunwaldt J-D, Damsgaard C D, Wellenreuther G, Falkenberg G and Schroer C G 2013 High-resolution chemical imaging of gold nanoparticles using hard x-ray ptychography *Appl. Phys. Lett.* **102** 203104
[14] Yu Y-S *et al* 2018 Three-dimensional localization of nanoscale battery reactions using soft x-ray tomography *Nat. Commun.* **9** 921
[15] Gao Z *et al* 2021 Sparse Ab initio x-ray transmission spectrotomography for nanoscopic compositional analysis of functional materials *Sci. Adv.* **7** eabf6971
[16] Crowther R A, DeRosier D J and Klug A 1970 The reconstruction of a three-dimensional structure from projections and its application to electron microscopy *Proc. R. Soc. A* **317** 319–40
[17] Andersen A and Kak A 1984 Simultaneous algebraic reconstruction technique (sart): A superior implementation of the art algorithm *Ultrason. Imaging* **6** 81–94
[18] Kronig R d L 1926 On the theory of dispersion of x-rays *J. Opt. Soc. Am. A* **12** 547–57
[19] Kramers H A 1927 La diffusion de la lumiere par les atomes *Atti Cong. Intern. Fis. Como* **2** 545–57 (available at: www.lorentz.leidenuniv.nl/IL-publications/sources/Kramers_27.pdf)
[20] Flenner S, Kubec A, David C, Storm M, Schaber C F, Vollrath F, Müller M, Greving I and Hagemann J 2020 Hard x-ray nanoholotomography with a Fresnel zone plate *Opt. Express* **28** 37514–25
[21] Cloetens P, Ludwig W, Baruchel J, Van Dyck D, Van Landuyt J, Guigay J P and Schlenker M 1999 Holotomography: quantitative phase tomography with micrometer resolution using hard synchrotron radiation x rays *Appl. Phys. Lett.* **75** 2912–4
[22] Cloetens P, Barrett R, Baruchel J, Guigay J-P and Schlenker M 1996 Phase objects in synchrotron radiation hard x-ray imaging *J. Phys. D: Appl. Phys.* **29** 133
[23] Salditt T, Osterhoff M, Krenkel M, Wilke R N, Priebe M, Bartels M, Kalbfleisch S and Sprung M 2015 Compound focusing mirror and x-ray waveguide optics for coherent imaging and nano-diffraction *J. Synchrotron Radiat.* **22** 867–78
[24] Sprenger P, Stehle M, Gaur A, Gänzler A M, Gashnikova D, Kleist W and Grunwaldt J-D 2018 Reactivity of Bismuth molybdates for selective oxidation of propylene probed by correlative operando spectroscopies *ACS Catal.* **8** 6462–75
[25] Klag L, Baumgarten L, Gaur A, Sheppard T L and Grunwaldt J-D 2024 Comparison of structure and reactivity of hydrothermally prepared Bi-Mo-Co-Fe-O catalysts in selective propylene and isobutene oxidation *ChemCatChem* **16** e202301470
[26] Töpperwien M, van der Meer F, Stadelmann C and Salditt T 2018 Three-dimensional virtual histology of human cerebellum by x-ray phase-contrast tomography *Proc. Natl Acad. Sci.* **115** 6940–5
[27] Bartels M, Krenkel M, Haber J, Wilke R N and Salditt T 2015 X-ray holographic imaging of hydrated biological cells in solution *Phys. Rev. Lett.* **114** 048103
[28] Salditt T *et al* 2026 X-ray waveguide optics at GINIX/P10 PETRA III: recent progress and future directions *J. Synchrotron Radiat.* **33** 298–313
[29] Tustison N J *et al* 2021 The ANTsX ecosystem for quantitative biological and medical imaging *Sci. Rep.* **11** 9068
[30] Hagemann J *et al* 2021 Single-pulse phase-contrast imaging at free-electron lasers in the hard x-ray regime *J. Synchrotron Radiat.* **28** 52–63
[31] Nieuwenhove V V, Beenhouwer J D, Carlo F D, Mancini L, Marone F and Sijbers J 2015 Dynamic intensity normalization using eigen flat fields in x-ray imaging *Opt. Express* **23** 27975–89
[32] Dora J, Möddel M, Flenner S, Schroer C G, Knopp T and Hagemann J 2024 Artifact-suppressing reconstruction of strongly interacting objects in x-ray near-field holography without a spatial support constraint *Opt. Express* **32** 10801–28
[33] Ravi N *et al* 2024 SAM 2: segment anything in images and videos

[34] Dora J, Möddel M, Flenner S, Reimers J, Zeller-Plumhoff B, Schroer C G, Knopp T and Hagemann J 2025 Model-based autofocus for near-field phase retrieval *Opt. Express* **33** 6641–57
[35] Paganin D M 2006 *Coherent X-ray Optics*, (*Oxford Series on Synchrotron Radiation*) (Oxford University Press)
[36] Calvin S 2013 *Xafs for Everyone* (CRC Press)
[37] Nassi M, Brody W R, Medoff B P and Macovski A 1982 Iterative reconstruction-reprojection: an algorithm for limited data cardiac-computed tomography *IEEE Trans. Biomed. Eng.* **BME-29** 333–41
[38] Hendriksen A A, Schut D, Palenstijn W J, Viganó N, Kim J, Pelt D M, van Leeuwen T and Batenburg K J 2021 Tomosipo: fast, flexible and convenient 3D tomography for complex scanning geometries in Python *Opt. Express* **29** 40494–513
[39] van Aarle W, Palenstijn W J, Cant J, Janssens E, Bleichrodt F, Dabravolski A, Beenhouwer J D, Batenburg K J and Sijbers J 2016 Fast and flexible x-ray tomography using the ASTRA toolbox *Opt. Express* **24** 25129–47
[40] van Heel M and Schatz M 2005 Fourier shell correlation threshold criteria *J. Struct. Biol.* **151** 250–62
[41] Schroer C G *et al* 2018 PETRA IV: the ultralow-emittance source project at DESY *J. Synchrotron Radiat.* **25** 1277–90
[42] Johannes G *et al* 2026 Near-field nano holographic tomography with chemical contrast explotiting low-dimensionality constraints (https://doi.org/10.5281/zenodo.20552992)